Flow Turbulence Combust (2017) 98:417–443
DOI 10.1007/s10494-016-9764-z

Numerical Analysis of the Impact of the Interior Nozzle Geometry on Low Mach Number Jet Acoustics

Mehmet Onur Cetin[1] · Seong Ryong Koh[1] · Matthias Meinke[1,2] · Wolfgang Schröder[1,2]

Received: 1 April 2016 / Accepted: 25 August 2016 / Published online: 18 September 2016

Abstract The flow and acoustic fields of subsonic turbulent hot jets exhausting from three divergent nozzles at a Mach number $M = 0.12$ based on the nozzle exit velocity are conducted using a hybrid CFD-CAA method. The flow field is computed by highly resolved large-eddy simulations (LES) and the acoustic field is computed by solving the acoustic perturbation equations (APE) whose acoustic source terms are determined by the LES. The LES of the computational domain includes the interior of the nozzle geometry. Synthetic turbulence is prescribed at the inlet of the nozzle to mimic the exit conditions downstream of the last turbine stage. The LES is based on hierarchically refined Cartesian meshes, where the nozzle wall boundaries are resolved by a conservative cut-cell method. The APE solution is determined on a block structured mesh. Three nozzle geometries of increasing complexity are considered, i.e., the flow and acoustic fields of a clean geometry without any built-in components, a nozzle with a centerbody, and a nozzle with a centerbody plus struts are computed. Spectral distributions of the LES based turbulent fluctuated quantities inside the nozzle and further downstream are analyzed in detail. The noise sources in the near field are noticeably influenced by the nozzle built-in components. The centerbody nozzle increases the overall sound pressure level (OASPL) in the near field with respect to the clean nozzle and the centerbody-plus-strut nozzle reduces it compared to the centerbody nozzle due to the increased turbulent mixing. The centerbody perturbed nozzle configurations generate a remarkable spectral peak at $St = 0.56$ which also occurs in the APE findings in the near field region. This tone is generated by large scale vortical structures shed from the centerbody. The analysis of the individual noise sources shows that the entropy term possesses the highest acoustic contribution in the sideline direction whereas the vortex sound source dominates the downstream acoustics.

✉ Mehmet Onur Cetin
o.cetin@aia.rwth-aachen.de

[1] Institute of Aerodynamics, RWTH Aachen University, Wüllnerstraße 5a, 52062 Aachen, Germany

[2] Forschungszentrum Jülich, JARA – High-Performance Computing, 52425 Jülich, Germany

Keywords Large-eddy simulation · Acoustic perturbation equation · Computational aeroacoustics · Multi-shear-layer flow · Nozzle built-in components

1 Introduction

Since jet noise is one of the major noise contributors of the overall engine noise, its reduction is a research area of remarkable interest. To comply with the new noise level regulations released in the European ACARE 2050 targets, i.e., the reduction of the noise level by 65 %, efficient and accurate aeroacoustic predictions are required. Appreciable progress has been achieved over the last 20 years in the decrease of jet noise by using various noise reduction techniques such as high bypass ratio and design variations on the nozzle casing. These techniques have primarily focused on increasing the turbulent mixing by altering the nozzle design. In modern engines, the bypass ratio has already reached the limiting value and any further increase will aggravate the engine performance. Therefore, any additional noise reduction technique could concentrate on the flow control inside the nozzle by using nozzle built-in components such as wedges, vanes etc. to influence the flow development and the sound radiation. However, the prediction of the noise sources generated by those built-in components is a quite challenge due to their geometric intricacy.

Aerodynamically generated jet noise comprises two major sources [1]. The large-scale turbulence structures are seen in the downstream of the nozzle exit associated with the low-frequency noise, whereas the small-scale turbulence structures are located in the vicinity of the nozzle exit and forming the near-field acoustics at high frequencies. These turbulent scales are remarkably altered by the nozzle geometry and its built-in components resulting in different nozzle exit conditions. Speth and Gaitonde [2] analyzed the impact of the boundary layer thickness of supersonic jets and showed that a jet with a thin boundary layer has a higher sound pressure level than a thick boundary layer jet. Bogey and Bailly [3] studied the influence of the momentum thickness on the sound field for initially laminar subsonic jets. They discovered that the level of high frequency humps associated with vortex pairing noise grows when the momentum thickness is increased. Furthermore, the pairing noise moves to higher frequencies when the initial boundary layer thickness decreases. Bogey and Marsden [4] investigated the effect of nozzle exit boundary layer thickness for highly disturbed subsonic jets where the peak turbulent intensity is around 9 %. They found that for constant diameter based Reynolds number jets, increasing the initial momentum thickness results in approx. 3 dB noise reduction at 90 degree radiation angle. This means that to accurately predict the sound radiation the nozzle built-in components, which impact the nozzle exit conditions, must be taken into account.

In the following, the literature on the influence of built-in components on the flow and acoustic field will be discussed. Note that serrations and chevrons are not considered built-in components since they are located in the nozzle exit such that those results will not be reported on. Papamoschou [5] experimentally analyzed the impact of the Fan Flow Deflection (FFD) method, where the flow field is controlled to suppress the noise in the near field. It was found that this method is efficient for the reduction of the mixing noise, especially in the downward direction of the jet axis. Johnson *et al.* [6] investigated the the fan flow deflectors with an adjoint method for aerodynamic shape optimization, where 50 deflector configurations with variable chord length, angle of attack, and azimuthal angle of the vanes for a supersonic jet with a high bypass ratio nozzle were considered. They reported that positioning the vanes at lower azimuthal angles resulted in a better noise reduction in the downward direction. Furthermore, a 1-2 degree difference in the angle of attack resulted

in 2 dB noise level variation. At optimum vane design parameters they achieved a noise reduction of approx. 3 dB in the downward direction and a somewhat lower reduction in the sideline direction compared to a baseline configuration. Papamoschou and Shupe [7] explored experimentally the acoustic performance of the fan flow deflectors that are used for noise reduction. They compared the performance of the configurations with wedges and vanes. Both components showed a superior acoustic performance in a nozzle design which generates convergent flow lines between the core and the bypass plumes compared to a nozzle with parallel flow lines. Henderson *et al.* [8] performed measurements to analyze the impact of the nozzle vanes on the jet noise reduction. They found that the angle of attack and the axial position of the vanes are essential parameters. Especially the low frequency noise was influenced by the vane position.

Another noise suppression method is the so-called offset stream technology (OST) concept, where the jet flow is controlled using wedges, vanes, and S-ducts resulting in a remarkable noise reduction especially in the jet near field. Brown *et al.* [9] found that OST designs can control and alter the flow field azimuthally such that the noise level from the core can be reduced on one side of the jet, where the flow is deflected, whereas the noise is increased on the opposite side. The directional noise control was achieved by using different types of nozzle built-in components. An S-duct configuration, for example, reduced the noise level at the far field. Additionally, they discovered that this directional noise control showed a higher performance at lower bypass ratio. They concluded that the OST concept has a potential for noise reduction at certain flight conditions.

Similarly, offset stream nozzles at different operating conditions were numerically investigated by Dippold *et al.* [10]. They found that inclusion of the S-duct and vanes resulted in a reduction of the peak value of the turbulence intensity by 11 % and 10 % in the downward direction of the jet axis and an increase of 60 % for the S-duct nozzle and 33 % for the vane nozzle in the opposite direction of the jet with a thrust penalty of less than 0.5 %. This provides an acoustic shielding effect by thickening the jet plume in the downward direction at take-off condition. They concluded that the vane type and S-duct type nozzle built-in components are appropriate design tools to redirect the sound propagation with a noticeable noise reduction without strongly aggravating the aerodynamic performance of the jet engine. Furthermore, an experimental study to reduce the noise level by modified nozzle designs was carried out by Saiyed *et al.* [11]. They introduced tabs on the core and fan of the nozzle, i.e., on the outer casing of the nozzle. The tabs reduced the overall noise level significantly without having a thrust penalty and the tabs on the core of the nozzle resulted in a better aeroacoustic performance than the tabs on the fan nozzle. They also found that the effective perceived noise level (EPNL) reduction grows for high thrust values for the nozzles with tabs compared to a baseline configuration. A joint experimental and numerical study on the control of the jet plume with beveled nozzles was successfully carried out by Viswanathan *et al.* [12]. They investigated the deflection of the jet stream by ranges of bevel angles and reported a noise reduction in the aft angles. The optimum deflection angle which provides the best acoustic performance and lowest thrust loss was in a range between 24-30 degree. Beveled nozzles resulted in a small increase in the noise level (1 dB) at lower polar angles, however, a large noise reduction (3-4 dB) was observed at higher polar angles. Overall, a net noise reduction was obtained by the modified nozzle configurations for different beveling angles.

Real nozzle configurations often contain internally mixed multi-shear-layer flows. Those multiple jet streams influence the noise level in the near field quite dramatically. Bridges [13] experimentally reported the impact of the dual-stream jet on the acoustic field. The peak frequency and directivity of the noise generated by a supersonic jet are influenced

by the alteration of the internal shear layer of the jet. The acoustic field of a twin converging-diverging nozzle was numerically analyzed using LES in [14] resulting in a 3 dB peak noise reduction. From the previous studies, it can be concluded that the nozzle built-in components can be used for noise suppression. However, since they can also increase the noise level at certain locations, it is necessary to carefully assess the impact of the nozzle built-in components.

This study concentrates on the analysis of the effect of the geometric details inside the nozzle on the flow field and the acoustic field. Three nozzle geometries will be analyzed. One nozzle configuration contains a centerbody and another configuration consists of a centerbody plus struts such that compared to a clean configuration without any built-in components additional shear layers and wakes are generated whose effects on the acoustic field will be investigated. Such geometric variations will influence the noise generation in the near field. That is, unlike previous studies where the exit velocity distribution was prescribed [15–17] the nozzle geometry is included in the simulation domain in the current analysis. First, the flow field is computed by a highly resolved LES and then, the acoustic field is determined by solving the APE whose source terms are determined by the LES findings.

This manuscript is structured as follows. First, the numerical methods are presented. Then, the flow problems, i.e., the nozzle geometries and flow parameters are defined. Subsequently, the results with emphasis on the turbulent flow fields and the acoustic fields are presented and finally, some conclusions are drawn.

2 Numerical Method

2.1 Flow field

The governing equations are the non-dimensional Navier-Stokes equations for unsteady, compressible flow

$$\int_V \frac{\partial \mathbf{Q}}{\partial \mathbf{t}} \, \mathrm{d}V + \oint_A \overline{\mathbf{H}} \cdot \mathbf{n} \, \mathrm{d}A = \mathbf{0} \quad , \tag{1}$$

where $\mathbf{n}$ is the normal vector of the surface $\mathrm{d}A$, $\mathbf{Q} = [\rho, \rho\mathbf{u}, \rho E]^T$ is the vector of conservative variables with the density ρ, velocity vector $\mathbf{u}$, and the total specific energy $E = e + \mathbf{u}^2/2$ containing the internal specific energy e. The flux vector $\overline{\mathbf{H}}$ contains the inviscid $\overline{\mathbf{H}}^i$ and the viscous part $\overline{\mathbf{H}}^v$

$$\overline{\mathbf{H}} = \overline{\mathbf{H}}^i + \overline{\mathbf{H}}^v = \begin{pmatrix} \rho\mathbf{u} \\ \rho\mathbf{u}\mathbf{u} + p \\ \mathbf{u}(\rho E + p) \end{pmatrix} + \frac{1}{\mathrm{Re}_0} \begin{pmatrix} \mathbf{0} \\ \overline{\tau} \\ \overline{\tau}\mathbf{u} + \mathbf{q} \end{pmatrix} \quad . \tag{2}$$

The Reynolds number is defined by the fluid properties at rest denoted by the subscript 0, $\mathrm{Re}_0 = \rho_0 a_0 l_{ref}/\eta_0$, where a_0 is the speed of sound and l_{ref} the characteristic length. The dynamic viscosity η_0 is calculated using Sutherland's law. Assuming a Newtonian fluid and neglecting the volume viscosity the shear stress $\overline{\tau}$ can be expressed by

$$\overline{\tau} = \frac{2}{3}\eta \left(\nabla \cdot \mathbf{u}\right) \overline{\mathbf{I}} - \eta \left(\nabla\mathbf{u} + (\nabla\mathbf{u})^T\right) \quad . \tag{3}$$

The vector of heat conduction $\mathbf{q}$ is formulated according to Fourier's law where T is the temperature

$$\mathbf{q} = -\frac{k}{\mathrm{Pr}\,(\gamma-1)}\nabla T \quad . \tag{4}$$

The quantity k is the thermal conductivity, the Prandtl number is $\mathrm{Pr} = \eta_0 c_p/k_0$, where c_p is the specific heat at constant pressure, and γ the ratio of specific heats. The thermal conductivity at constant Prandtl number is $k(T) = \eta(T)$.

The system of equations is closed by the equation of state for an ideal gas

$$e = \frac{p}{\rho\,(\gamma-1)} \quad . \tag{5}$$

For the LES, the monotone integrated LES (MILES) approach [18] is adopted, i.e., the dissipative part of the truncation error of the numerical method mimics the dissipation of the non-resolved subgrid scale stresses. This solution method has been validated and successfully used, e.g., in [19–22].

2.2 Acoustic field

The acoustic perturbation equations (APE) are applied to determine the sound propagation and to identify the dominant noise sources. Since a compressible flow problem is considered, the APE-4 system is used [23]. The acoustic perturbation equations were derived from the continuity and Navier-Stokes equations. Using an expression for the excess density $\rho_e = (\rho-\overline{\rho})-(p-\overline{p})/\overline{a^2}$, where the overbar denotes mean quantities, the rearranged APE-4 system [24] reads

$$\frac{\partial p'}{\partial t} + \overline{a^2}\nabla\cdot\left(\overline{\rho}\mathbf{u}' + \overline{\mathbf{u}}\,\frac{p'}{\overline{a^2}}\right) = \overline{a^2}(q_c + q_e) \tag{6}$$

$$\frac{\partial \mathbf{u}'}{\partial t} + \nabla\left(\overline{\mathbf{u}}\cdot\mathbf{u}'\right) + \nabla\left(\frac{p'}{\overline{\rho}}\right) = \mathbf{q}_m \quad . \tag{7}$$

The right-hand side source terms are

$$q_c = -\nabla\cdot\left(\rho'\mathbf{u}'\right)' \,, \tag{8}$$

$$q_e = -\frac{\partial \rho_e}{\partial t} - \nabla\cdot\left(\rho_e\overline{\mathbf{u}}\right) \,, \tag{9}$$

$$\mathbf{q}_m = -(\omega\times\mathbf{u})' - \left(\nabla\frac{|\mathbf{u}'|^2}{2}\right)' + \nabla\frac{p'}{\overline{\rho}} - \left(\frac{\nabla p}{\rho}\right)' , \tag{10}$$

where the source q_c denotes the nonlinear compressibility effect, the entropy source q_e describes the acoustic contribution of the entropy fluctuations, and the momentum source q_m includes the vortex sound source, the nonlinear effect of the turbulent kinetic energy, and the interaction of the entropy fluctuations with the time-averaged pressure distribution. The excess density represents the difference between the density and the pressure perturbation at an analogous acoustic medium whose density perturbation is isentropic and the sound speed is a [25].

The first step of the hybrid method is based on an LES for the turbulent jet flow to provide the data of the noise source terms Eqs. 8, 9, and 10. Then, the corresponding acoustic field is computed by solving the acoustic perturbation Eqs 6 and 7.

2.3 Spatial and temporal discretization

The Navier-Stokes equations are solved on a fixed non-isotropic locally refined hierarchical Cartesian grid using a cell-centered finite-volume discretization. The mesh is generated by a fully parallel mesh generator with hierarchical mesh refinement [26]. At wall boundaries, cut cells are introduced. That is, cells which intersect the surface $\partial\Gamma$ are cut by computing their cutting points with the Standard Tessellation Language (STL) describing the surface of the nozzle and discarding the part which is located outside of the domain Γ such that the boundary $\partial\Gamma$ is approximated by piecewise linear segments. Based on the cutting points, the new volume, surface areas, and boundary-surface normals of the cut cell can be computed. Furthermore, the cell-center is shifted to the new center of gravity of each cell. For further details, the reader is referred to [27].

The surface fluxes are computed using an upwind-biased scheme. The primitive variables at the cell surfaces are obtained by a second-order accurate monotonic upstream-centered scheme for conservation laws (MUSCLs) scheme, where the left and right values at each surface centroid are extrapolated from the cell-centers of the two facing cells.

For the computation of the inviscid flux vector a modified version of the advection upstream splitting method (AUSM) in a low dissipation version suitable for LES proposed by Meinke *et al.* [21] is used. For the explicit temporal integration a second-order accurate 5-stage Runge-Kutta scheme [28] is used.

The aforementioned cut-cell approach can produce arbitrary small cells, which can lead to numerical instabilities. To ensure stability without reducing the time step to extremely small values, a flux redistribution method is applied. This flux redistribution approach was developed in [29] where the details of the formulation are given.

To accurately resolve the acoustic wave propagation described by the acoustic perturbation equations in the APE-4 formulation [24] a sixth-order finite difference scheme with the summation by parts property [30] is used for the spatial discretization and an alternating 5-6 stage low-dispersion and low-dissipation Runge-Kutta method for the temporal integration [31]. On the embedded boundaries between the inhomogeneous and the homogeneous acoustic domain an artificial damping zone has been implemented to suppress spurious sound generated by the acoustic-flow-domain transition [32]. A detailed description of the two-step method and the discretization of the Navier-Stokes equations and the acoustic perturbation equations is given in [33].

2.4 Boundary conditions

First, the boundary conditions of the flow simulation are discussed. The inlet of the computational domain is located downstream of the last turbine stage. For the formulation of the inflow boundary condition of the time averaged values, the operating conditions are taken from the measurements of a full scale turbo-shaft engine test at high power of 900 kW [34]. The same mass flow $\dot{m} = 3.49 kg/m^3$ and operating temperature are prescribed at the inlet for the three nozzle configurations. Isotropic synthetic turbulence is superimposed to the mean flow field at the inlet plane with approx. 10 % turbulence intensity [35] to mimic the turbulence field downstream of the last turbine stage entering the simulation domain through the inlet section. The synthetic turbulence generation ensures a divergence-free velocity field where a perturbed velocity field is added to the constant mean inflow which meets the prescribed Reynolds-stress tensor on average. The perturbed velocity field contains individual Fourier modes who possess random amplitudes and frequency. Random fluctuations are only introduced at the inlet plane and after a transient region a natural development

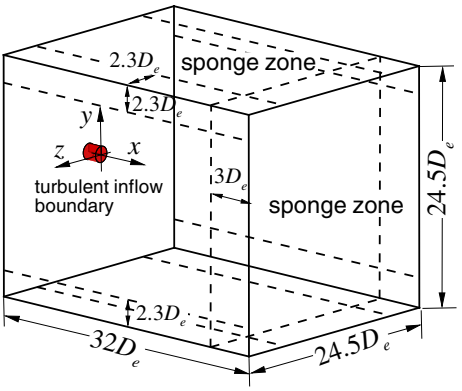

Fig. 1 Schematic of the computational domain of the flow field; D_e is the nozzle exit diameter

of turbulence is obtained. For more details, the reader is referred to [36]. A zero-pressure gradient normal to the inlet surface is applied and the density profile is determined by the Crocco-Busemann relation [37].

At the nozzle wall, an adiabatic wall is assumed and the no-slip condition with a zero-pressure gradient is imposed. For the outflow and lateral exterior boundaries of the jet domain, the static pressure is set constant and all other variables are extrapolated along linearized characteristics from the interior domain. To prevent any spurious wave reflection on the boundaries, sponge layers are prescribed [38]. Figure 1 illustrates the computational domain with the axial and radial extents of the sponge zones.

For the acoustic computations, non-reflecting boundary conditions [39] are prescribed at the boundaries of the computational domain.

3 Problem Definition

3.1 Nozzle geometry and computational meshes

Figure 2 shows the interior of three variants of the engine nozzle, the clean nozzle hj_1, the centerbody nozzle hj_2, and the centerbody-plus-strut nozzle hj_3 which are identical except for the centerbody and the struts which support the centerbody. The geometric notations are given in Fig. 3. The nozzle expansion ratio R_e/R_i is 1.3125, where $R_e = D_e/2$ is the

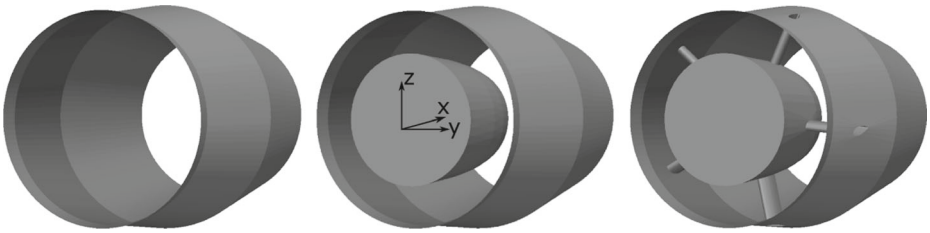

Fig. 2 Rear section of the nozzle geometry (a) clean nozzle hj_1, (b) centerbody nozzle hj_2, (c) centerbody-plus-strut nozzle hj_3.

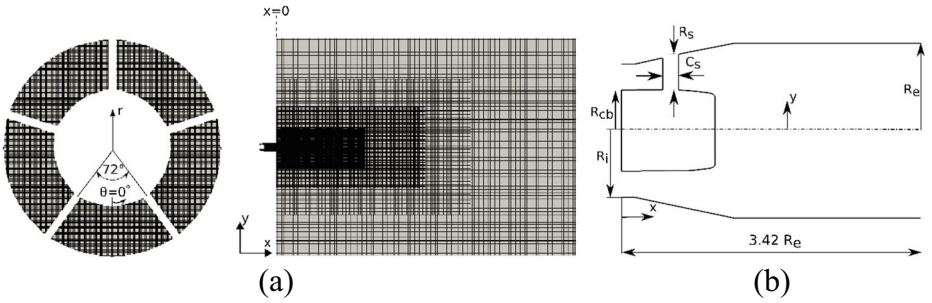

Fig. 3 (**a**) Cartesian flow-field mesh for the centerbody-plus-strut nozzle hj_3, left: cross section view at $x/R_e = -2.88$, right: complete computational domain in the x-y plane with 6 refinement levels, for clarity not all of them are shown, decreasing in the axial and radial direction, (**b**) sketch of the near section of the centerbody-plus-strut nozzle hj_3

nozzle exit radius and $R_i = D_i/2$ is the nozzle inlet radius, and the ratio of the radii of the centerbody and the exit cross section is $R_{cb}/R_e = 0.42$. The ratio of the chord length and the maximum radial extent of the strut is $C_s/R_s = 0.46$ and the maximum thickness of the strut profile is $0.079R_e$. The 5 struts possess an airfoil-like shape and are equidistantly distributed over the circumference. The overall axial extent of the nozzle geometry is $3.42R_e$.

The LES meshes are generated by the Cartesian mesh generator developed by Lintermann *et al.* [26]. The minimum cell lengths in the x-, y-, and z- direction are $\Delta x = \Delta y = \Delta z = 0.00297D_e$, where D_e is the nozzle exit diameter. In wall units, the grid spacing corresponds to $\Delta x^+ = \Delta y^+ = \Delta z^+ \approx 5.5$ at the nozzle exit. Note that due to the special formulation of the boundary cut cells no stairstep-like but a perfectly smooth surface is simulated [29]. The overall jet domain has an extent of $32D_e$ and $24.5D_e$ in the streamwise and the radial direction. The right figure in Fig. 3(a) shows the Cartesian mesh used for the centerbody-plus-strut nozzle configuration containing 328 million cells and the left figure illustrates a radial cross section inside the nozzle where also the struts are present.

Figure 4 shows the computational domain to determine the acoustic field. The noise source region in which Eqs. 8, 9, and 10 of the APE are determined, extends $8.7D_e$ in the axial direction and $2.3D_e$ in the sideline direction. The acoustic perturbation equations are solved on a domain which extends $24D_e$ in the axial direction and $27D_e$ in the sideline direction.

The minimum/maximum spatial step of $0.024R_e/0.53R_e$ in the sideline direction and the constant spacing of $0.024R_e$ in the jet direction of the source region result in approx. 108.5 million cells to resolve the acoustic field. The time step is $\Delta t = 0.011R_e/a_\infty$. Based on the summation by parts dispersion relation preserving scheme the spectral resolution in the wavenumber space requires at least 5 points per wavelength λ. Consequently, on the present acoustic mesh the maximum Strouhal number $St = fD_e/u_e$ based on the frequency f, the nozzle exit diameter D_e, and the mean axial exit velocity u_e is approximately $St_{\max} = 3$ where the mean wavelength $\overline{\lambda}$ is 5 times the grid spacing at a position ($x = 15R_e$, $y = 11R_e$) of the acoustic domain.

3.2 Flow parameters

The flow parameters are identical for the various nozzle configurations. The Mach number $M_j = \frac{u_e}{a_\infty} = 0.12$ is defined based on the mean axial nozzle exit velocity u_e and the

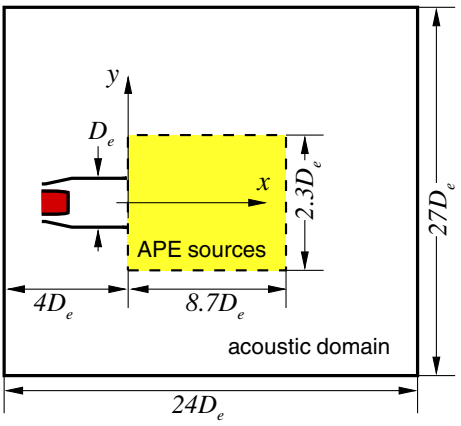

Fig. 4 Schematic of the acoustic computational domain in the $x - y$ plane, —— APE domain, – – – acoustic source region, D_e is the nozzle exit diameter

ambient speed of sound a_∞. The Reynolds number $Re_{D_e} = \frac{\rho_e u_e D_e}{\eta_e}$ slightly varies for the three nozzle configurations due to the different temperature distributions at the nozzle exit. It is defined based on the nozzle exit conditions, where ρ_e is the average density, D_e nozzle exit diameter, and η_e dynamic viscosity.

The Reynolds number for the clean nozzle configuration is $Re_{D_e} = 332,936$, for the centerbody nozzle configuration $Re_{D_e} = 316,578$, and for the centerbody-plus-strut nozzle configuration $Re_{D_e} = 318,503$. The essential mesh and simulation parameters of the analysis of the flow and the acoustic fields are summarized in Table 1.

4 Results

In this section, the results from the three nozzle configurations are discussed in detail. The LES and APE methods were validated in [22, 40] and the mean flow field was thoroughly analyzed in [22]. Therefore, only a concise discussion of the averaged flow field of the three nozzle configurations is given, before spectral distributions of the turbulent components at several streamwise locations are investigated and then, the acoustic fields are discussed.

4.1 Flow field

In the following, the flow field of the three nozzle configurations is discussed. Simulations are run long enough to ensure a statistically converged, fully developed turbulent flow field. The total simulation time is 128 D_e/u_e with a time step 1.6×10^{-4} D_e/u_e and 2251 LES snapshots are used to average the flow field. Additionally, spectral analyses of the time signals recorded for 70 D_e/u_e convective time units of the pressure and radial velocity fluctuations are discussed to understand the aerodynamically generated noise sources emitted in the jet near field.

4.1.1 Time-averaged flow field

The nozzle built-in components have a large influence on the jet characteristics downstream of the nozzle exit. This is illustrated by the mean axial velocity contours in Fig. 5. The

Table 1 Simulation features and mesh parameters of the flow and the acoustic field solutions

	Clean nozzle (hj_1)	Centerbody nozzle (hj_2)	Centerbody-plus-strut nozzle (hj_3)
Flow field			
Mach number M_j	0.12	0.12	0.12
Reynolds number Re_{D_e}	332,936	316,578	318,503
Mesh points	335×10^6	329×10^6	328×10^6
Min. streamwise cell length	Δx=0.00297D_e	Δx=0.00297D_e	Δx=0.00297D_e
Simulation time	128 D_e/u_e	128 D_e/u_e	128 D_e/u_e
Sampling time	70 D_e/u_e	70 D_e/u_e	70 D_e/u_e
Number of samples	2251	2251	2251
Acoustic field			
Mesh points	108.5 x 10^6	108.5 10^6	108.5 x 10^6
Simulation time	638 D_e/a_∞	638 D_e/a_∞	638 D_e/a_∞

velocity decay in the clean nozzle hj_1 configuration is much weaker than that of the centerbody nozzle hj_2 and the centerbody-plus-strut nozzle hj_3. The centerbody in the hj_2, hj_3 configurations generates a wake which lowers the velocity on the center of the jet. A secondary wake is also visible downstream of the strut for the hj_3 configuration which results in an asymmetric velocity distribution in the jet near field. The development of the mean axial velocity normalized by the average nozzle exit axial velocity

$$u_e = \frac{1}{A}\int \mathbf{u}\cdot\vec{n}dA \quad , \tag{11}$$

which is 0.1156, 0.1218, and 0.1211 for the hj_1, hj_2, and hj_3, is illustrated in Fig. 6 on the nozzle centerline. The clean nozzle configuration has a decaying profile between $-2.3 < x/R_e < -1.1$ due to the divergence of the nozzle geometry. However, downstream of $x/R_e = -1.1$ the hj_1 configuration possesses a standard free jet velocity distribution whose unperturbed core ends further downstream than that of the centerbody nozzle configurations. The nozzle built-in components influence the flow field such that downstream of the centerbody a negative velocity distribution sets in due to the flow recirculation. Further downstream, the velocity distributions of the hj_2 and hj_3 configurations reach their maximum at around $x/R_e \simeq 6$ and both profiles are alike at $x/R_e \geqslant 12$. In other words, the impact of the struts on the jet centerline velocity is effective up to 12 radii downstream of the nozzle exit. Further downstream all profiles almost match at approx. $x/R_e \geqslant 35$.

The streamwise distributions of the root mean square (rms) axial and radial velocities on the centerline are illustrated in Fig. 7. Note that the notation radial velocity, which is used throughout the paper, defines the velocity component normal to the streamwise direction in the z=0, x-y plane. The clean nozzle configuration possesses much lower axial turbulence intensity than that of the hj_2 and hj_3 configurations at $x/R_e \leqslant 14$. That is, the nozzle built-in components in the hj_2 and hj_3 configurations increase the turbulence intensity in the jet near field. Additionally, downstream of the nozzle exit the hj_3 configuration possesses 25 % lower turbulence intensity than the hj_2 configuration. The struts excite a stronger azimuthal mixing which reduces the maximum intensity of the axial velocity fluctuations. Figure 7(b) illustrates the centerline distribution of the rms radial velocity. Again, the clean

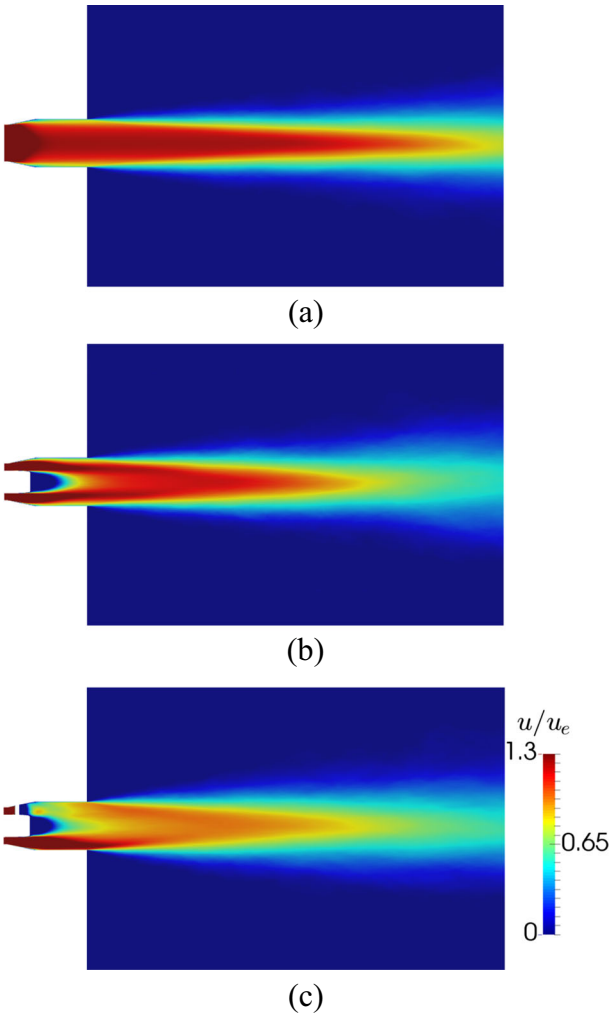

Fig. 5 Contours of the mean axial velocity u/u_e in the free jet region for three nozzle geometries (a) hj_1, (b) hj_2, (c) hj_3

Fig. 6 Streamwise distribution of the mean normalized axial velocity on the nozzle centerline for (—) hj_1, (− −) hj_2, (-·-) hj_3

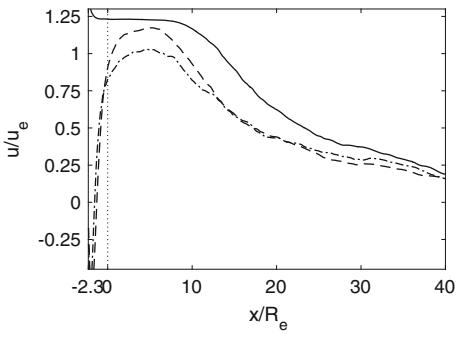

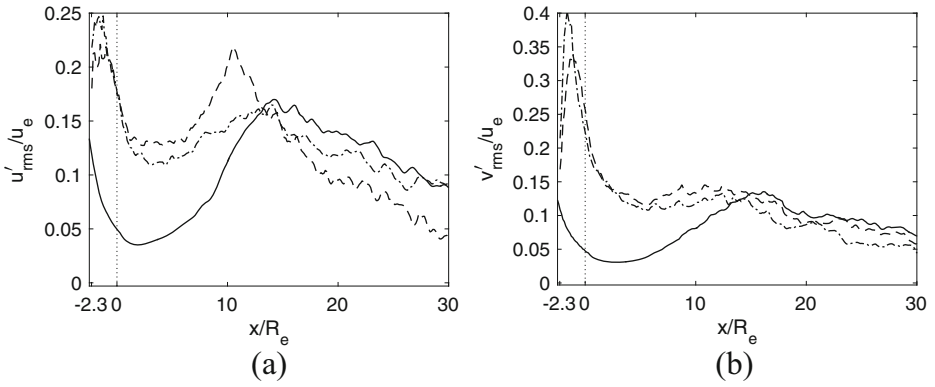

Fig. 7 Streamwise distributions of the rms (a) axial velocity, (b) radial velocity on the nozzle centerline for (—) hj_1, (− −) hj_2, (-·-) hj_3

nozzle configuration has a much lower turbulence intensity at $x/R_e \leqslant 14$. The peak value of the hj_3 configuration inside the nozzle is larger than that of the hj_2 configuration. This indicates that the radial velocity fluctuations generated by the wake of the struts amplify the fluctuations generated by the centerbody wake. All profiles almost coincide for $x/R_e \geqslant 15$ indicating that the impact of the nozzle built-in components is minor beyond this region.

4.1.2 Analysis of the turbulent quantities in the near field

To give an overall impression of the flow structure of the turbulent jets instantaneous vorticity contours are illustrated in Fig. 8. This qualitative comparison shows that the built-in components in the hj_2, hj_3 solutions enhance the turbulent mixing in the jet near field yielding a larger spreading rate.

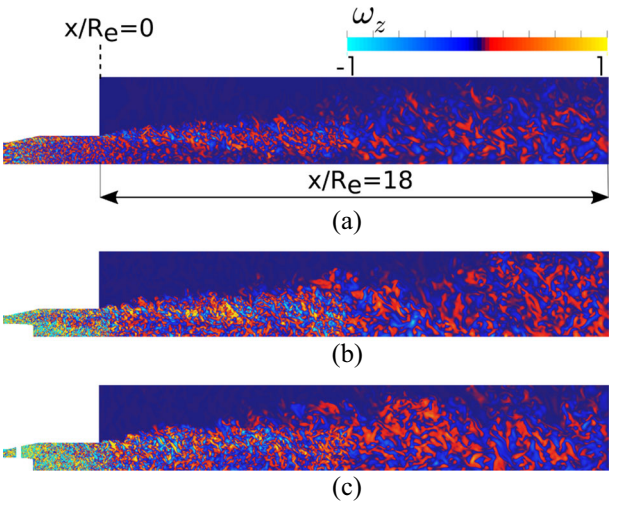

Fig. 8 Contours of the instantaneous distribution of the vorticity component in the z-direction in an x-y plane for three geometries (a) hj_1, (b) hj_2, (c) hj_3

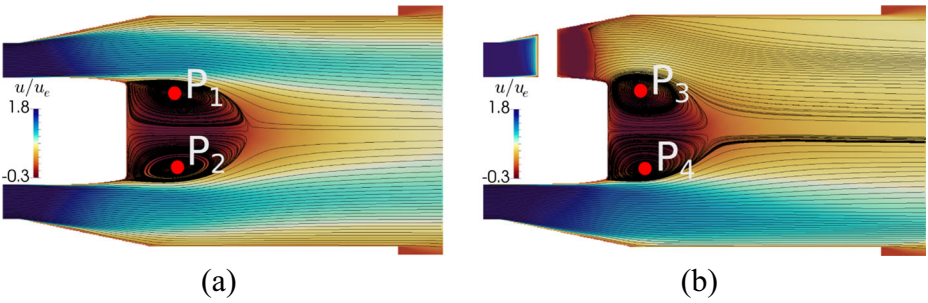

Fig. 9 Streamlines in the rear part inside the nozzle (a) hj_2, (b) hj_3.

The spectral state and the temporal correlations inside the nozzle are considered at four pressure probe positions P_1, P_2, P_3, P_4 defined in Fig. 9, where also the streamlines of the mean flow field in the x-y plane inside the nozzle for the centerbody configurations hj_2, hj_3 are illustrated. The probes are located in the center of the recirculation zones right downstream of the centerbody. For the Power Spectral Density (PSD) distributions of the data sequence of the 2251 samples Welch's algorithm with Hanning windowing and 50 % overlapping is used. The number of overlapping time sequences is 2 and based on the Nyquist criterion the minimum Strouhal number is $St = 0.02$. PSD distributions of the pressure fluctuations at the upper half of the jet at P_1 and P_3 are shown in Fig. 10(a). It is clear from the distributions that for the hj_2 configuration a peak $St = 0.56$ is generated at P_1, while for the hj_3 configuration another peak $St = 0.71$ occurs at P_3. Figure 10(b) displays the PSD distributions at the counter positions P_2 and P_4 in the lower half of the jet. Due to the axisymmetry the same spectral peak at P_2 is visible for the hj_2 configuration at $St = 0.56$.

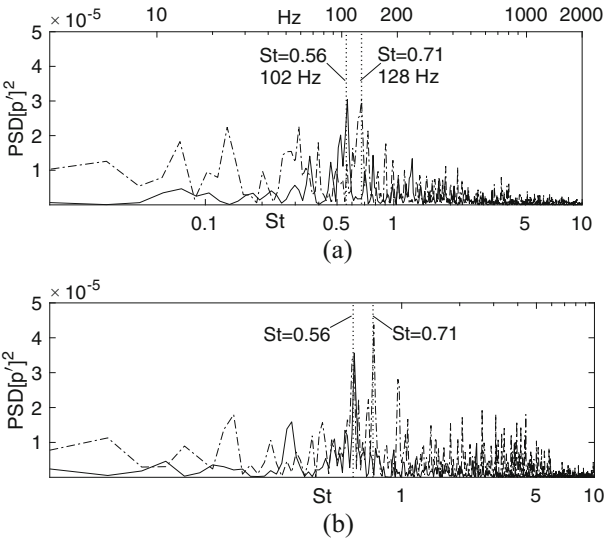

Fig. 10 Power spectral density of the pressure fluctuations at the points shown in Fig. 9 (a) P_1 (—), and P_3 (···), (b) P_2 (—), and P_4 (···). Figure 10(a) shows a Hz-scale distribution based on the approx. conversion ratio Hz/St=180

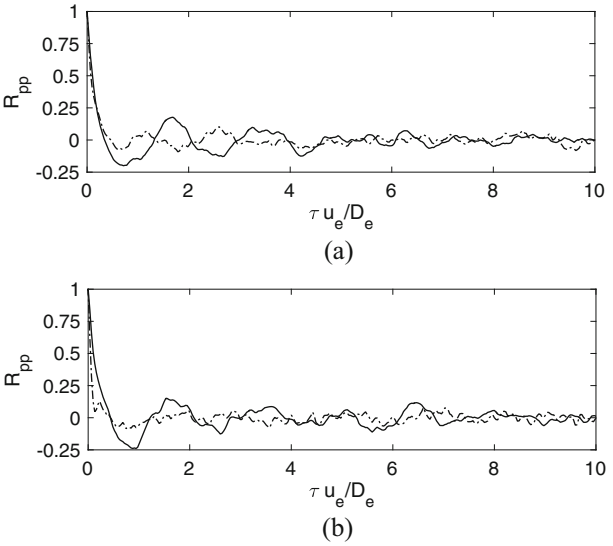

Fig. 11 Auto-correlation distributions of the pressure fluctuations R_{pp} at the points shown in Fig. 9 (a) P_1 (—), and P_3 (-·-), (b) P_2 (—), and P_4 (-·-)

For the hj_3 configuration, however, two peaks $St = 0.56$ and $St = 0.71$ are observed at P_4. Hence, due to the presence of the struts the frequency of the pressure fluctuations is determined by the wake of the struts ($St = 0.71$) and the free-shear layer shed from the centerbody ($St = 0.56$).

The temporal auto-correlation distributions of the pressure fluctuations

$$R_{pp}(\tau) = \frac{< p'(t)p'(t+\tau) >}{< p'^2(t) >} \tag{12}$$

of the four pressure probes inside the nozzle are depicted in Fig. 11. Whereas the P_1 and P_2 distributions, i.e., the hj_2 configuration, confirm the axisymmetry of the wake, the differences in the P_3 and P_4 distributions emphasize the strong interaction of the wakes of the struts and the centerbody. The wavelengths of the P_1 and P_2 distributions of the hj_2 configuration evidence its large scale coherent structures.

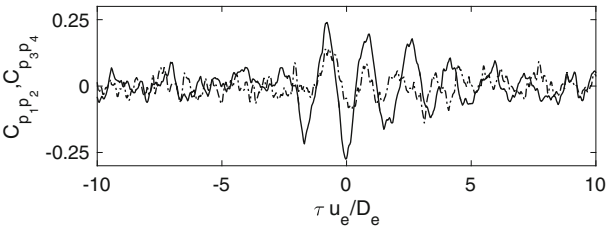

Fig. 12 Cross-correlation distributions of the pressure fluctuations at the points shown in Fig. 9 for $C_{p_1p_2}$ (—), $C_{p_3p_4}$ (-·-)

The temporal cross-correlation distributions of the hydrodynamic pressure fluctuations between the points P_1, P_2 and P_3, P_4

$$C_{p_1p_2}(\tau) = \frac{< p_1'(t)p_2'(t+\tau) >}{< p_1'(t)p_2'(t) >} \quad , C_{p_3p_4}(\tau) = \frac{< p_3'(t)p_4'(t+\tau) >}{< p_3'(t)p_4'(t) >} \tag{13}$$

are shown in Fig 12. It is evident from the distributions that the counter points, i.e., P_1, P_2 for the hj_2 configuration and P_3, P_4 for the hj_3 configuration, are negatively correlated due to the phase shift of the shedding vortices right downstream of the centerbody.

To further understand the variation of the spectral content in the radial and the azimuthal directions, the PSD distributions of the radial velocity fluctuations for the three configurations are determined at two radial locations in the exit cross section in Figs. 13, 14 and 15. To be more precise, the locations defined in Fig. 3(a) are at $x/R_e = 0$, $\theta = 0^\circ$, and $r/R_e = 0.225$ in the inner wake as well as $r/R_e = 0.75$ in the outer wake region. A peak is detected at $St = 0.56$ in Fig. 13 for the hj_2 solution which does not occur in the hj_1 and hj_3 distributions, i.e., the centerbody generates this peak value and the struts suppress it in the $\theta = 0^\circ$ plane. Note that the amplitude of the distribution of the hj_1 solution at $r/R_e = 0.225$ is scaled by a factor of 20 to be able to compare all solutions.

To further analyze the impact of the struts, besides the $\theta = 0^\circ$ plane the $\theta = 36^\circ$ plane, which is also defined in Fig. 3(a), for the hj_3 configuration is considered at the nozzle exit in Fig. 14. It is clear from Fig. 14(a) which shows the PSD distributions close to the center of the jet at $r/R_e = 0.225$ that no peak occurs for $\theta = 0^\circ$ at $St = 0.56$ but one at $St = 0.38$ in the wake of the strut. However, Fig. 14(b) clearly shows that the $St = 0.56$ peak is generated in the $\theta = 36^\circ$ plane.

Figure 15 illustrates the PSD distributions at 2 radii downstream of the nozzle exit. In Fig. 15(a) the spectral peak at $St = 0.56$ again occurs in the hj_2 solution. Additionally, we

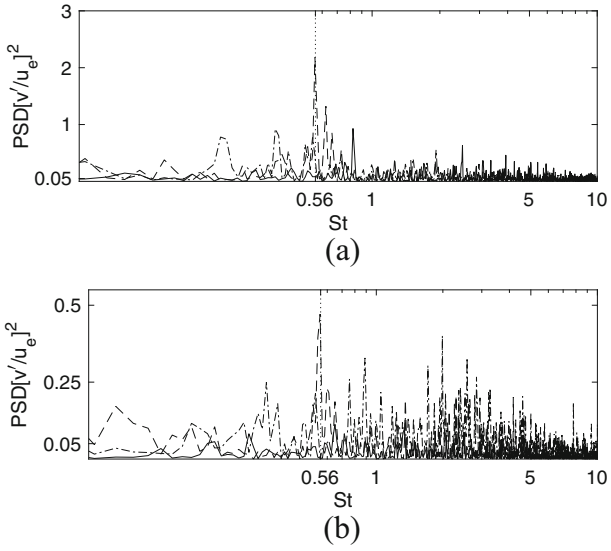

Fig. 13 Power spectral density of the fluctuations of the radial velocity component at the nozzle exit $x/R_e = 0, \theta = 0^\circ$ (a) $r/R_e = 0.225$, (b) $r/R_e = 0.75$ for (—) hj_1, (– –) hj_2, (-·-) hj_3. Note that PSD distribution of the hj_1 solution at $r/R_e = 0.225$ is scaled by a factor of 20

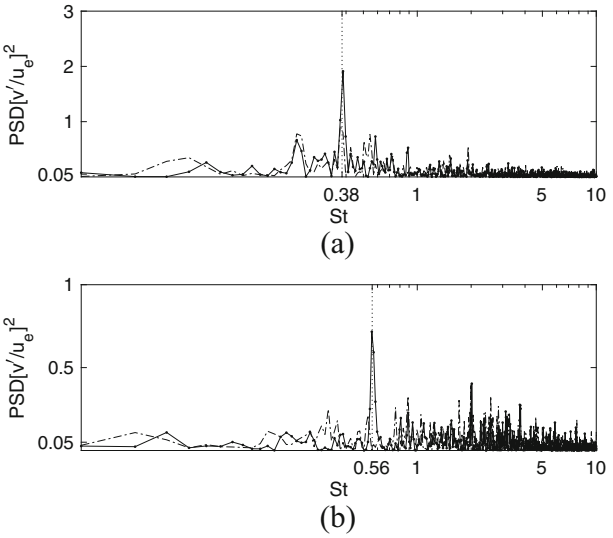

Fig. 14 Power spectral density of the fluctuations of the radial velocity component of the hj_3 solution at the nozzle exit $x/R_e = 0$ (a) $r/R_e = 0.225$, (b) $r/R_e = 0.75$ for (---) at $\theta = 0°$, (—•—) at $\theta = 36°$

assume the other peak at $St = 0.59$ for the hj_1 configuration to be generated by a free-shear layer instability downstream of the nozzle exit since the momentum thickness at 2 radii downstream of the nozzle exit corresponds to the value of the momentum thickness that is based on u_e. For the hj_3 configuration the $St = 0.56$ peak is observed at $\theta = 36°$ in Fig. 15(b).

Azimuthally averaged PSD distributions 10 radii downstream of the nozzle exit at r/R_e=1.5 are displayed in Fig. 16. All spectra display a similar decaying behavior. However, the centerbody perturbed nozzle configurations hj_2 and hj_3 reveal a slightly larger amplitude over the whole frequency range compared to the clean nozzle configuration.

The analysis of the PSD distributions of the fluctuations of the radial velocity component shows a clear peak value at $St = 0.56$ for the hj_2 solution, which is caused by the shed vortices downstream of the centerbody. This peak value still occurs in the hj_3 solution when the distribution in the wake region of the struts is considered. The disturbances in the azimuthal direction caused by the struts weaken the vortex shedding downstream of the centerbody such that the emanating vortices are less strong in the $St = 0.56$ range. At 10 radii downstream of the nozzle exit the peak disappears.

The pressure fluctuations of the flow field are analyzed by considering the pressure level contours in dB scale at several locations. The contours at the nozzle exit $x/R_e = 0$ on the circle $r/R_e = 0.225$ show a strong contribution in the range $0 < St < 2$ for the hj_2 solution in Fig. 17.

A peak at $St = 0.56$ is noticeable for the contours displayed at the nozzle exit $x/R_e = 0$ for a larger radius $r/R_e = 0.75$ in Fig. 18. For the hj_3 solution, periodic pressure oscillations occur in the nozzle exit at an approximate interval of $\Delta\theta = 72°$ due to the struts and further downstream at $x/R_e = 2$ which is shown in Fig. 19. These structures are more evident in the higher Strouhal number region $St > 5$. Unlike the hj_3 geometry, the hj_1 and hj_2 configurations have smooth circumferential distributions. Moreover, the same peak (cf. Fig. 15(a)) at approx. $St \simeq 0.59$ is observed for the hj_1 configuration.

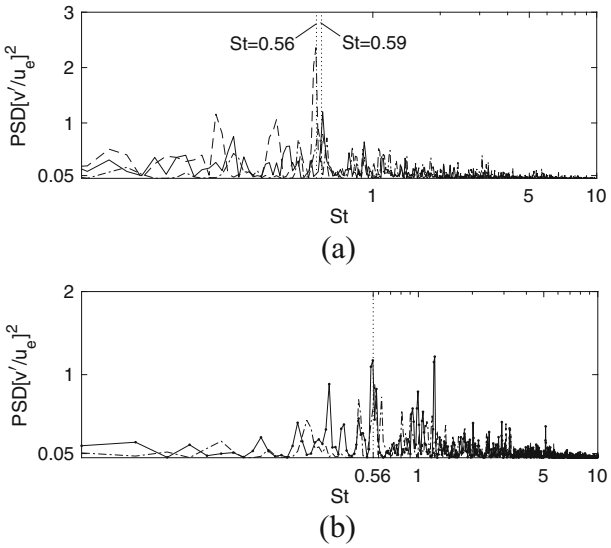

Fig. 15 Power spectral density of the fluctuations of the radial velocity component at $x/R_e = 2$, $r/R_e = 1$ (a) $\theta = 0^\circ$ for (—) hj_1, (− −) hj_2, (·-·) hj_3, (b) $\theta = 0^\circ$ for (·-·) hj_3, $\theta = 36^\circ$ for (—•—) hj_3

The distributions 10 radii downstream of the nozzle exit are illustrated in Fig. 20. The periodic oscillation caused by the struts for the hj_3 configuration is removed in this plane over the whole frequency range. The hj_1 configuration reveals a slightly lower spectral magnitude than the centerbody configurations. Finally, azimuthally averaged PSD distributions at $x/R_e = 10$ are shown in Fig. 21, where the centerbody nozzle hj_2 configuration possesses the highest magnitude over a broad frequency range, while the hj_1 jet has the lowest contribution indicating that this configuration generates the least acoustic energy among the three nozzle configurations.

4.2 Acoustic field

The discussion of the acoustic results focuses on two aspects. In the first part, the geometry impact on the noise generation is addressed for the three jet configurations hj_1, hj_2, and hj_3.

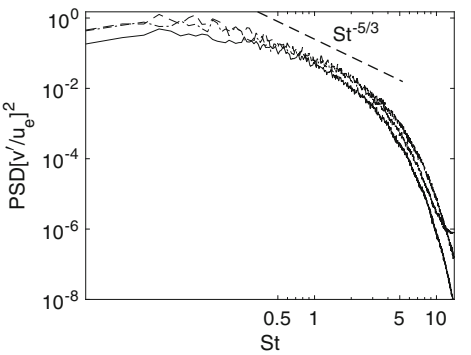

Fig. 16 Azimuthally averaged PSD distributions of the fluctuations of the radial velocity component at $x/R_e = 10$ and $r/R_e = 1.5$ for (—) hj_1, (− −) hj_2, (·-·) hj_3

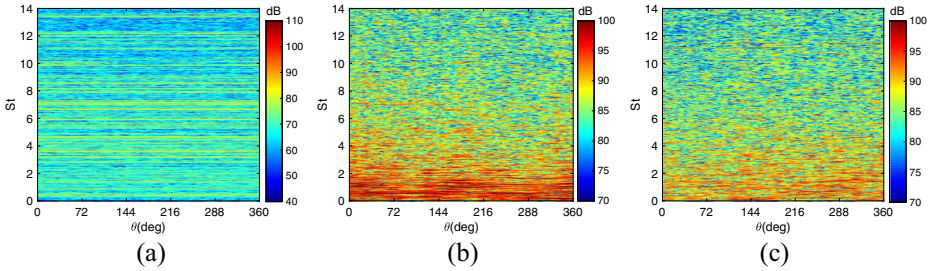

Fig. 17 Pressure level contours at the nozzle exit on the circle $r/R_e = 0.225$ for (a) hj_1, (b) hj_2, (c) hj_3

The major difference in the acoustic field is analyzed using the overall sound pressure level and the sound spectra of the sideline and the downstream direction. In the second part, the acoustic analysis considers the impact of the heat-excited noise source on the acoustic field. The discussion contains the detailed sound spectra obtained by the three noise sources, i.e., the nonlinear, the entropy, and the momentum source of the APE-4 system.

4.2.1 Geometry impact on noise generation

The acoustic analyses include the sound waves whose maximum wavenumber $k_{\max} = 2\pi/\lambda_{\min}$ is approximately $0.36\pi/R_e$. The sources are provided by 2251 LES snapshots that correspond to the turbulent flow field over a time interval $T_{\text{total}} = 148.5R_e/u_e$. At each time step the acoustic source terms are consecutively reconstructed by 10 LES snapshots based on a least squares interpolation algorithm [41].

In Fig. 22 the contours of the acoustic pressure near the jet nozzle region in the range $|p'/\rho_0 a_0^2| \leqslant 5 \times 10^{-6}$ are illustrated. The acoustic pressure of the configuration hj_1 possesses smaller amplitudes than the configurations hj_2 and hj_3. Upstream and downstream of the nozzle exit the turbulent fluctuations are less pronounced for the hj_1 configuration compared to the hj_2 and hj_3 configurations as discussed in Fig. 7. This lower rms level is the major reason of the low acoustic energy in the hj_1 jet. For a subsonic jet, the sound power is proportional to the rms velocity variation by u_{rms}^4 [42]. The centerline distribution of the mean velocity fluctuations in Fig. 7 corroborates the lower acoustic emission of the hj_1 and hj_3 configurations compared to the hj_2 configuration.

The overall sound pressure level in Fig. 23 evidences the low acoustic emission of the hj_1 jet. The profiles of three acoustic fields are determined in the axial direction at the sideline location $8R_e$ off the jet centerline. The acoustic directivity of the hj_1 configuration

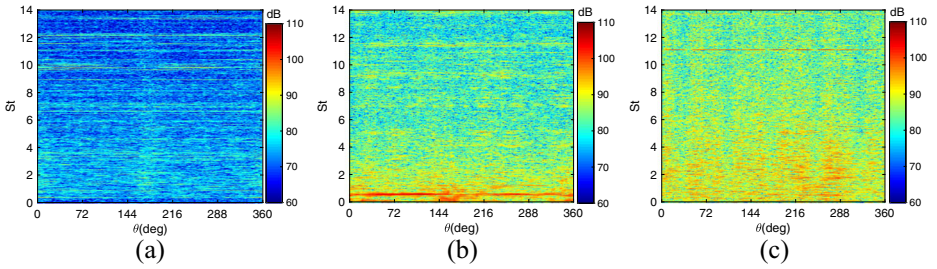

Fig. 18 Pressure level contours at the nozzle exit on the circle $r/R_e = 0.75$ for (a) hj_1, (b) hj_2, (c) hj_3

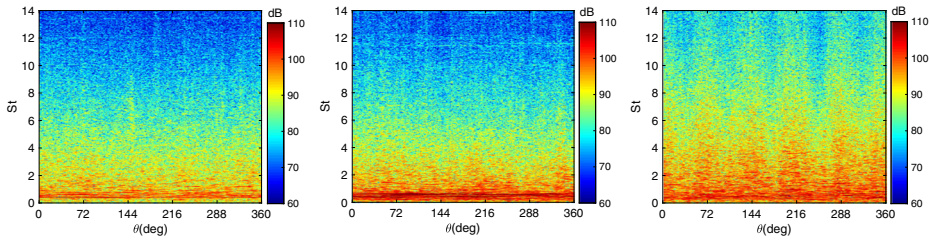

Fig. 19 Pressure level contours at $x/R_e = 2$ on the circle $r/R_e = 1$ for (a) hj_1, (b) hj_2, (c) hj_3

evidences a clear reduction in the upstream position $x \leqslant 5R_e$. Compared with the hj_1 findings the axial distributions of the hj_2 and hj_3 configurations show an approximately 2–9dB higher acoustic pressure. For the hj_1 configuration the dominant wave radiation occurs at the end of the potential core. The centerbody nozzle configuration hj_2 generates the most powerful acoustics which shows a 4dB higher OASPL at the streamwise position $x = 10R_e$ compared to the hj_1 jet. The additional turbulent mixing by the struts in the configuration hj_3 reduces the acoustic generation by approximately 2–4dB over the streamwise position $R_e \leqslant x \leqslant 19R_e$.

In Fig. 24 the acoustic spectra of the hj_1, hj_2, and hj_3 configurations are compared. The sound pressure is determined at the coordinates $x = 3R_e, r = 8R_e$ for the sideline acoustics in Fig. 24(a) and at $x = 18R_e, r = R_e$ for the downstream acoustics in Fig. 24(b).

All three configurations include the spectral hump in the frequency range $0.1 \leqslant St \leqslant 2$. The noise level and the frequency band vary for each jet configuration that has a different nozzle geometry. In the discussion of the jet noise spectra in [43], the high temperature ratio of a hot stream to the ambient flow contributes to the strong dipole generation which forms an acoustic hump in the frequency band. This noise generation is represented by the temperature (density) fluctuation terms.

In the current jet configurations a large increase of the power spectral density occurs in the sideline acoustics where the convection effect is minimum. The peaks are located at $St = 0.45$ for the hj_1 configuration and at $St \sim 0.6$ for the centerbody configurations hj_2 and hj_3. The flow separation by the centerbody generates a large acoustic hump compared to the hj_1 jet. The turbulence generation by the struts of the hj_3 jet reduces the peak level and curtails the frequency range of the spectral hump. The downstream acoustics in Fig. 24(b) shows the pronounced low frequency radiation at $St \leqslant 0.1$ for the hj_2 and the hj_3 configuration. The acoustic peaks occur at the same frequency range identified in the

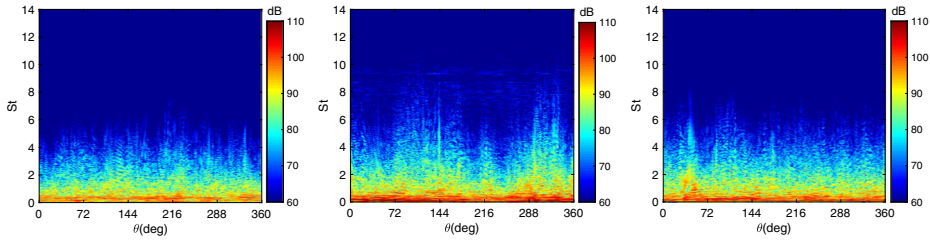

Fig. 20 Pressure level contours at $x/R_e = 10$ on the circle $r/R_e = 1.5$ for (a) hj_1, (b) hj_2, (c) hj_3

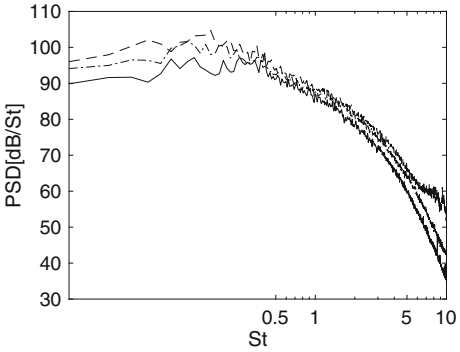

Fig. 21 Azimuthally averaged PSD distributions at $x/R_e = 10$ and $r/R_e = 1.5$ for (—) hj_1, (– –) hj_2, (-·-) hj_3

sideline acoustics. As indicated by the spectra of the hj_2 and hj_3 configurations the increase of the acoustic power becomes more prominent when the turbulent fluctuations increase as discussed in section 4.1.

The sound generation of the jets includes two sources. The first source is the downstream acoustics due to the large scale turbulence in the shear layers and the second source is the sideline acoustics enhanced by the temperature gradient. Figure 24(a) illustrates the differences of the sideline acoustics. The acoustic radiation almost perpendicular to the jet axis is clearly more intensified for the centerbody configurations hj_2 and hj_3 than that of the hj_1 configuration. Moreover, in the frequency range $0.1 \leqslant St \leqslant 0.5$ the acoustic level of the centerbody-plus-strut configuration hj_3 is reduced compared to that of the centerbody configuration hj_2. This is due to the smaller turbulent scales in the hj_3 wake which are caused by the interaction of the wake of the struts and the centerbody shear layer. The enhanced turbulence mixing by the struts was discussed for the distribution of the turbulence intensity on the centerline in Fig. 7. Inside the nozzle at $x \leqslant 0$ the configuration hj_3 possesses the peak of the velocity fluctuations severely intensified than those of the configurations hj_1 and hj_2. The interaction of the struts wake and the centerbody shear layer changes the development of the jet in the downstream of the nozzle exit and the convection of the corresponding acoustic sources.

4.2.2 Heat impact on noise generation

Next, the sound generation of the hj_1, hj_2, and hj_3 configurations is investigated with respect to the impact of the various noise sources. Based on the source terms in the APE-4 system the present analysis focuses on the decomposed acoustic sources. The source components are divided into three parts, i.e., the momentum $\mathbf{q}_m$, the entropy q_e, and the nonlinear q_c sources in Eqs. 6 and 7. The momentum source $\mathbf{q}_m$ in Eq. 10 consists of the fluctuations of the Lamb vector components, i.e., the vortex sound source, the thermodynamic fluctuations, and the nonlinear effects of the turbulent kinetic energy. In the detailed analysis of the individual sources in [17, 41], the entropy source possesses the major contribution to the noise generation of the hot jets due to the acoustic component induced by the temperature gradient.

In Fig. 25 the instantaneous source contours of the hj_1, hj_2, and hj_3 jets are presented. Excited by the temperature gradient in the shear layer, the heat components, i.e., q_c in

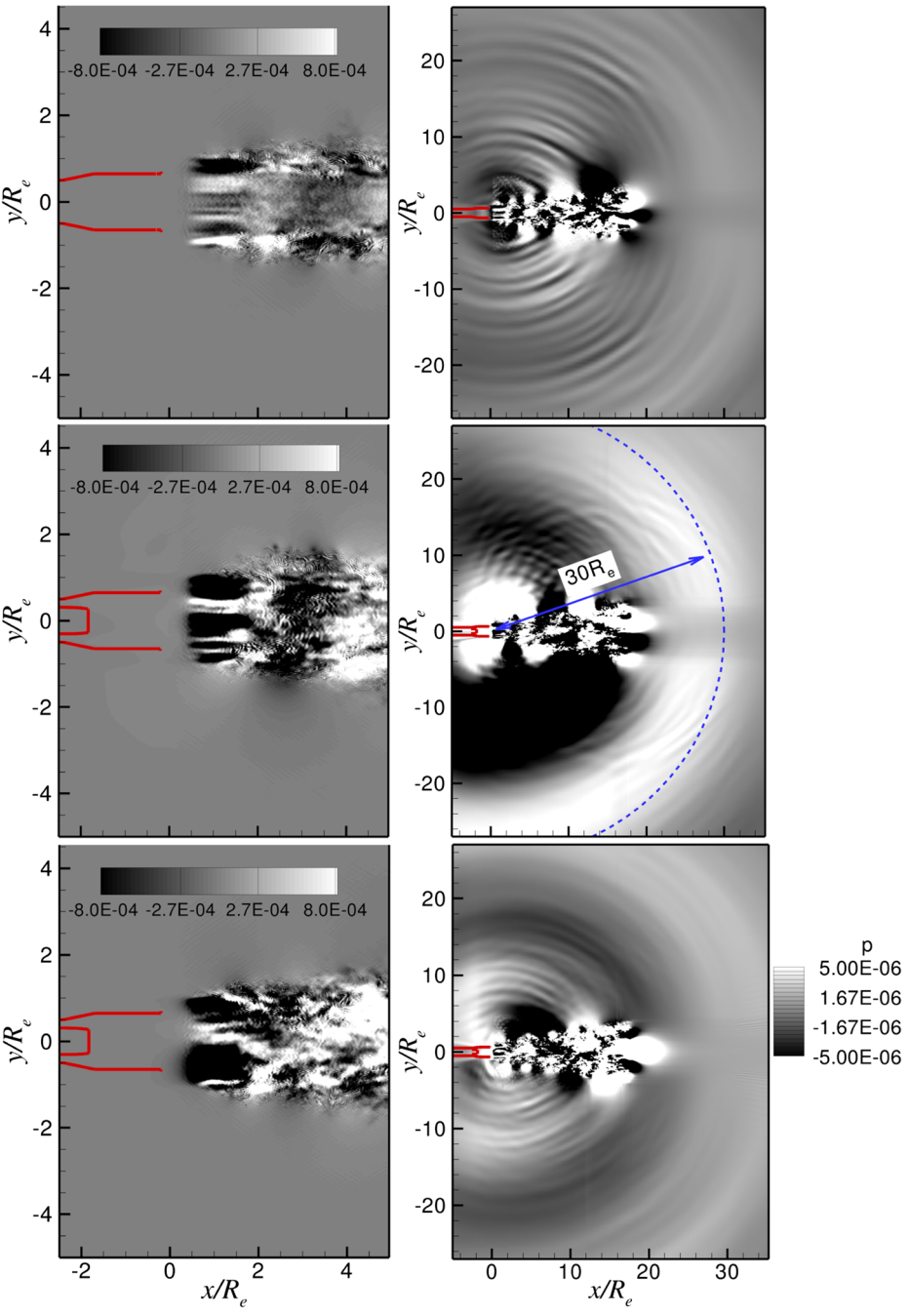

Fig. 22 Acoustic pressure contours in the range $|p'/\rho_0 a_0^2| \leqslant 5 \times 10^{-6}$ in the z=0 plane: hj_1(top), hj_2(center), hj_3(bottom); left column: enlarged near field, right column: total view

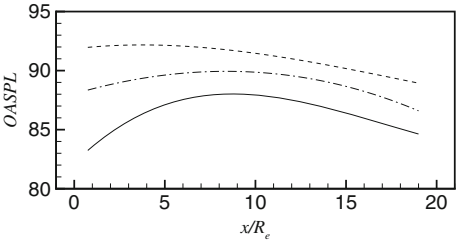

Fig. 23 Overall sound pressure level in dB at the radial distance of $8R_e$ from the jet centerline for (—) hj_1, (− −) hj_2, (-·-) hj_3.

Fig. 25(a) and q_e in Fig. 25(b), form a highly intensified region surrounding the axis of the jet. The contribution of the entropy source term q_e extends into the streamwise direction up to $x = 10R_e$. The substantial time derivative of the excess density fluctuations shows a pronounced turbulent mixing at the end of the inner hardly perturbed jet in Fig. 25(b). In Fig. 25(c) the intensity of the Lamb vector fluctuations is enhanced by the turbulent mixing in the core region upstream of the nozzle exit for the hj_2 and hj_3 jets. The vortex sound of the hj_2 and hj_3 configurations is primarily attributed to the centerbody impact on the turbulent structures inside the nozzle.

Figure 26 shows the acoustic contribution of various noise sources on the sound spectra. In the left column, the sound spectra of the sideline acoustics are presented. The slope of the broadband spectra determined by the momentum q_m possesses an f^{-1} decay in the frequency band between $St = 0.03$ and $St = 3$ for the hj_1 nozzle. The hj_2 and hj_3 nozzles show the spectral decay changing over the frequency band due to the centerbody, i.e., the sound spectra are altered from an $f^{-0.5}$ decay in the range $St < 0.5$ to an f^{-2} decay in the range of $St \simeq 1$. The momentum source, whose acoustic contribution is indicated by dashed lines, has a minor impact on the sideline acoustics. The centerbody nozzle configuration hj_2 has a peak at $St = 0.6$ for the acoustic field based on the q_m source term. The tone corresponds to the peak frequency of the velocity fluctuations in Fig. 13. However, the dominant acoustic source is excited by the pronounced temperature or density gradient such that the sound spectra obtained by the entropy source q_e denoted by the thin solid lines almost coincides with the level of the full source acoustic spectra shown by the thick solid lines. For the configurations hj_1 and hj_3 the entropy source causes the acoustic peak at $St = 0.45$. The acoustic field of the configuration hj_2 has a higher sound level in the range $0.2 \leqslant St \leqslant 0.7$ compared to the hj_1 due to the additional flow mixing by the centerbody. For the hj_3 configuration, the sound pressure level is slightly decreased.

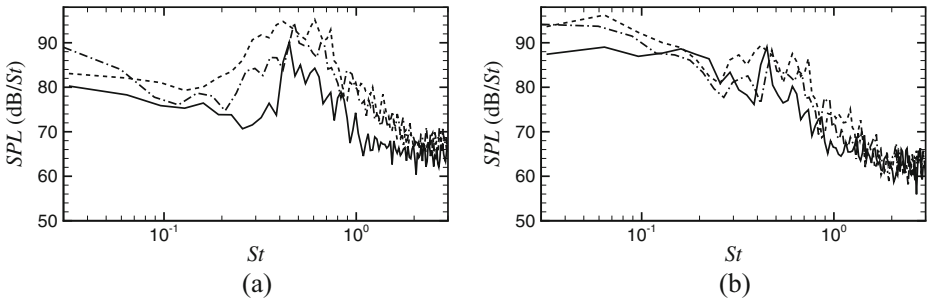

Fig. 24 Power spectra of the acoustic pressure signals determined at the coordinates (a) $x/R_e = 3$, $r/R_e = 8$ and (b) $x/R_e = 18$, $r/R_e = 8$ for (—) hj_1, (− −) hj_2, (-·-) hj_3

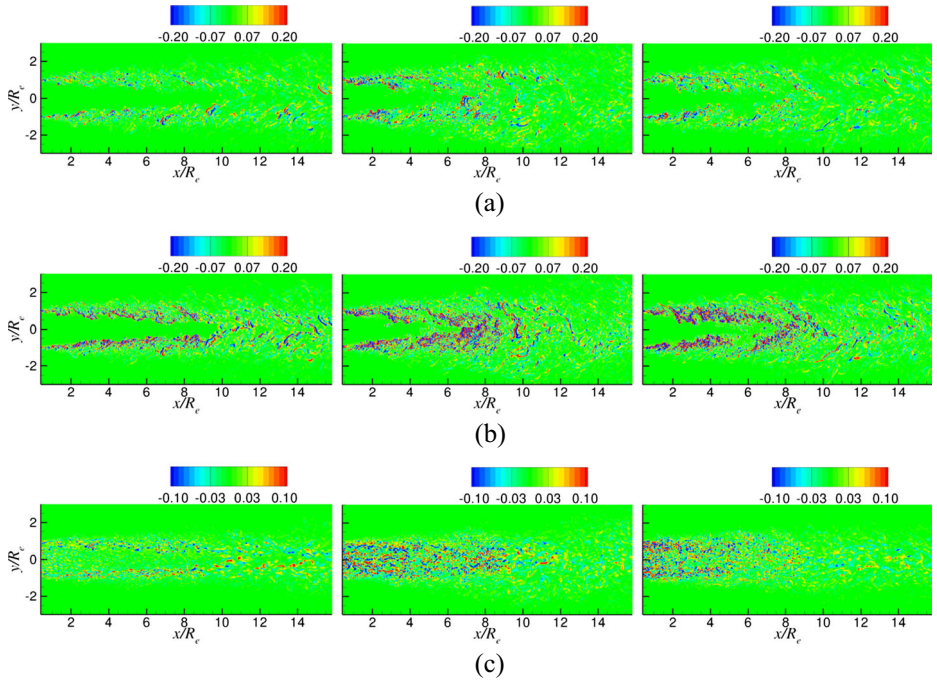

Fig. 25 Contours of the instantaneous noise sources of the hj_1 (left column), hj_2 (center column), and hj_3 (right column) jets, (a) nonlinear source q_c of Eq. 8 in the interval $\pm 0.2\rho_0 a_0/D_e$, (b) entropy source q_e of Eq. 9 in the interval $\pm 0.2\rho_0 a_0/D_e$, and (c) y-component of the vortex source $\mathbf{q}_m$ of Eq. 10 in the interval $\pm 0.1 a_0^2/D_e$

The downstream acoustics in the right column shows a f^{-2} slope in the frequency band $St \geqslant 0.1$. The momentum source dominates the acoustic generation at $St \leqslant 0.1$. However, over a wide range of the frequency band the downstream acoustics is again influenced by the entropy source. The comparison of the power spectra of the pressure fluctuations in Fig. 21 corroborates the powerful acoustic field in hj_2 and hj_3. When the acoustic fields of the hot jets are determined only by the momentum source ($\mathbf{q}_m$) its overall sound generation does not match the acoustic power considering the entropy and the nonlinear source. In other words, the spectral hump appears only with the entropy source terms since the vortex sound source is hardly impacted by the inhomogeneous density field which generates temperature fluctuations in the hot jets [17].

4.2.3 Summary of the acoustic results

In summary, the acoustic analysis of the hj_1, hj_2, and hj_3 jets shows that the overall sound generation is impacted by the turbulent mixing induced by the interaction of the large coherent flow structures with the centerbody and the struts. The centerbody in the hj_2 configuration is responsible for the large increase of the acoustic generation at the downstream of the nozzle exit. For the hj_3 configuration the wake generated by the struts prevents the strong flow separation by the centerbody such that in the acoustic field the overall sound pressure level decreases by 2–4dB compared to the hj_2 jet.

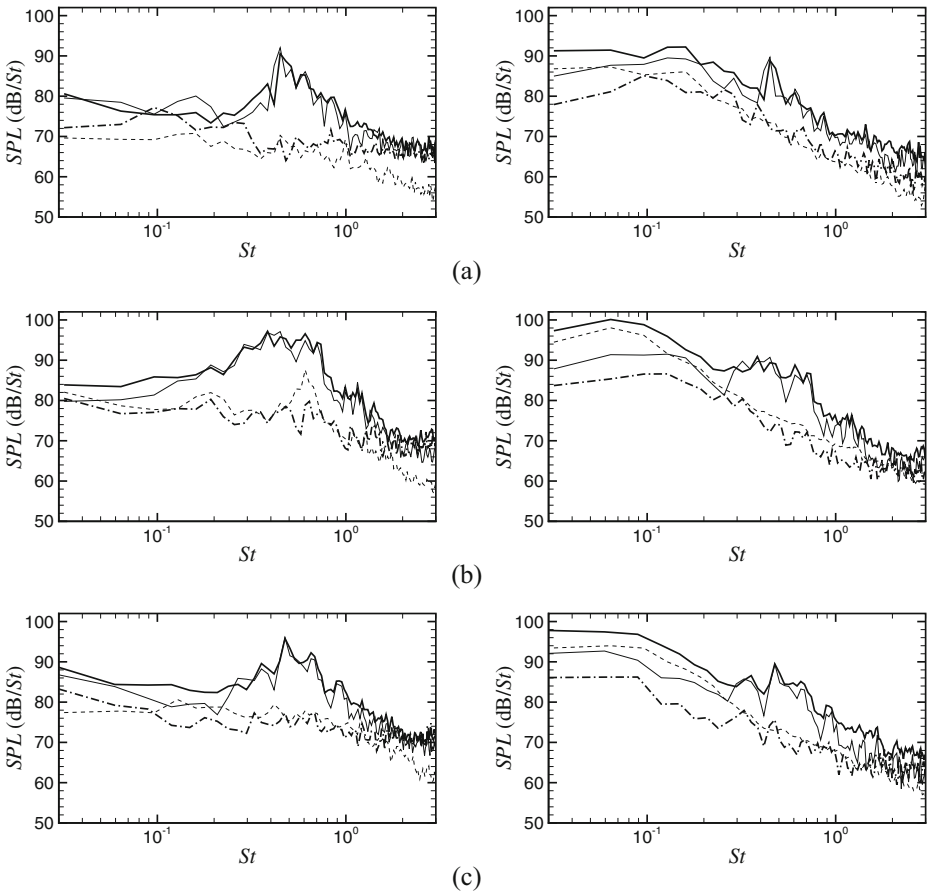

Fig. 26 Power spectra of the acoustic pressure signals determined at the coordinates $x/R_e = 3$, $r/R_e = 6$ (left column) and $x/R_e = 15$, $r/R_e = 6$ (right column) by the different source terms Eqs. 8, 9, 10 containing —— (q_c, q_e, and $\mathbf{q}_m$), —— (q_e), – – ($\mathbf{q}_m$), and ---- (q_c): (a) hj_1, (b) hj_2, (c) hj_3

The acoustic contribution of individual source terms is related to the momentum $\mathbf{q}_m$, the nonlinear q_c, and the entropy q_e source. The entropy source, which is intensified by the inhomogeneous density distribution of the jets due to the temperature gradient, determines the sideline acoustics whereas the momentum source possesses a negligible impact on the noise generation. For the downstream acoustics, the sound field is dominated by the large scale turbulent structures at the low frequencies. The spectral hump, which dominates the sideline acoustics is determined by the energy source term which is strongly influenced by the temperature gradient.

5 Conclusions

The flow field and the acoustic field of a subsonic jet including the nozzle geometry were predicted by a hybrid CFD/CAA method. First, the flow field was computed by an LES and subsequently, the acoustic field was determined by solving the APE. The acoustic source

terms consist of the nonlinear source of Eq. 8, the entropy source of Eq. 9, and the momentum source terms of Eq. 10. Three turbulent jets consisting of a clean divergent annular reference nozzle, a configuration with a centerbody and a geometry with a centerbody plus 5 azimuthally equidistantly distributed struts were considered. The Reynolds number was approx. Re $\simeq$ 320,000 and the Mach number M=0.12. First, the effect of the interior geometric variations on the turbulent flow fields was analyzed and then, the acoustic fields of the three nozzle configurations were discussed in detail by considering the contribution of different source terms.

The results showed an important dependence of the jet acoustic near field on the presence of the nozzle built-in components. The centerbody generated a rather broad hump in the acoustic spectra. The azimuthally correlated large scale coherent structures shed from the centerbody generated this broad region which is partly removed by the enhanced turbulent mixing excited by the struts. More precisely, the disturbances caused by the struts weaken the vortex shedding in the azimuthal direction downstream of the centerbody. That is, the struts increase the fluctuations generated by the centerbody wake and enhance the turbulent mixing which reduces the associated length scales that determine the peak at $St = 0.56$.

The analysis of the individual source terms showed that the acoustic field of the three nozzle configurations was dominated in the sideline direction by the entropy term which is determined by the pronounced temperature gradients and in the streamwise direction by the vortex sound source. The same spectral peak was found in the acoustic field at $St \simeq 0.6$ for the centerbody nozzle configuration as in the flow field. In the downstream acoustics the low frequency noise is dominated by the vortex sound source correlated with the large scale turbulence. This analysis of the flow field and the acoustic field led to the understanding of how the aeroacoustic sound is determined by the nozzle built-in components. On the one hand, the presence of the centerbody increased the OASPL up to 6 dB compared to the clean nozzle and on the other hand, the inclusion of the 5 struts decreased the OASPL up to 4 dB compared to the pure centerbody nozzle owing to the increased turbulent mixing caused by the struts which reduced the length and time scales of the turbulent structures shed from the centerbody.

Acknowledgments The research was funded from the European Community's Seventh Framework Programme (FP7, 2007-2013) PEOPLE program under the grant agreement No. FP7-290042 (COPAGT project). The authors gratefully thank the Gauss Centre for Supercomputing (GCS) for providing computing time for a GCS Large-Scale Project on the GCS share of the supercomputer JUQUEEN [44] at the Jülich Supercomputing Centre (JSC) and High Perfomance Computing Center Stuttgart (HLRS). GCS is the alliance of the three national supercomputing centres HLRS (Universität Stuttgart), JSC (Forschungszentrum Jülich), and LRZ (Bayerische Akademie der Wissenschaften) in Germany, funded by the German Federal Ministry of Education and Research (BMBF) and the German State Ministries for Research of Baden-Württemberg (MWK), Bayern (StMWFK) and Nordrhein-Westfalen (MIWF).

References

1. Tam, C.K.W.: Computational aeroacoustics-issues and methods. AIAA J. **33**(10), 1788–1796 (1995)
2. Speth, R.L., Gaitonde, D.V.: Nozzle-exit boundary-layer effects on a controlled supersonic jet. AIAA J. **53**(7), 2027–2039 (2015)
3. Bogey, C., Bailly, C.: Influence of nozzle-exit boundary-layer conditions on the flow and acoustic fields of initially laminar jets. J. Fluid Mech. **663**, 507–538 (2010)

4. Bogey, C., Marsden, O.: Identification of the effects of the nozzle-exit boundary-layer thickness and its corresponding reynolds number in initially highly disturbed subsonic jets. Phys Fluids (1994-present) **25**(5), 055106 (2013)
5. Papamoschou, D.: Fan flow deflection in simulated turbofan exhaust. AIAA J. **44**(12), 3088–3097 (2006)
6. Johnson, A.D., Xiong, J., Rostamimonjezi, S., Liu, F., Papamoschou, D.: Aerodynamic and acoustic optimization for fan flow deflection. AIAA Paper, 2011–1156 (2011)
7. Papamoschou, D., Shupe, R.S.: Effect of nozzle geometry on jet noise reduction using fan flow deflectors. AIAA Paper, 2006–2707 (2006)
8. Henderson, B., Norum, T., Bridges, J.: An MDOE assessment of nozzle vanes for high bypass ratio jet noise reduction. AIAA Paper, 2006–2543 (2006)
9. Brown, C., Bridges, J., Henderson, B.: Offset stream technology test–summary of results. AIAA Paper, 2007–3664 (2007)
10. Dippold, V.F., Foster, L.E., Wiese, M.R.: Computational analyses of offset-stream nozzles for noise reduction. J. Propuls. Power **25**(1), 204–217 (2009)
11. Saiyed, N.H., Mikkelsen, K.L., Bridges, J.: Acoustics and thrust of quiet separate-flow high-bypass-ratio nozzles. AIAA J. **41**(3), 372–378 (2003)
12. Viswanathan, K., Spalart, P.R., Czech, M.J., Garbaruk, A., Shur, M.: Tailored nozzles for jet plume control and noise reduction. AIAA J. **50**(10), 2115–2134 (2012)
13. Bridges, J.: Broadband shock noise in internally-mixed dual-stream jets. AIAA Paper, 2009–3210 (2009)
14. Brés, G.A., Bose, S.T., Ham, F.E., Lele, S.K.: Unstructured large eddy simulations for nozzle interior flow modeling and jet noise predictions. AIAA Paper, 2014–2601 (2014)
15. Freund, J.B.: Noise sources in a low-Reynolds-number turbulent jet at Mach 0.9. J. Fluid Mech. **438**, 277–305 (2001)
16. Bogey, C., Bailly, C., Juvé, D.: Noise investigation of a high subsonic, moderate Reynolds number jet using a compressible large eddy simulation. Theor. Comput. Fluid Dyn. **16**(4), 273–297 (2003)
17. Koh, S.R., Schröder, W., Meinke, M.: Turbulence and heat excited noise sources in single and coaxial jets. J. Sound Vib. **329**(7), 786–803 (2010)
18. Boris, J.P., Grinstein, F.F., Oran, E.S., Kolbe, R.L.: New insights into large eddy simulation. Fluid Dyn. Res. **10**(4-6), 199–228 (1992)
19. Alkishriwi, N., Meinke, M., Schröder, W.: Large-eddy simulation of streamwise-rotating turbulent channel flow. Comput. Fluids **37**(7), 786–792 (2008)
20. Renze, P., Schröder, W., Meinke, M.: Large-eddy simulation of film cooling flows at density gradients. Int. J. Heat Fluid Flow **29**(1), 18–34 (2008)
21. Meinke, M., Schröder, W., Krause, E., Rister, T.: A comparison of second-and sixth-order methods for large-eddy simulations. Comput. Fluids **31**(4), 695–718 (2002)
22. Cetin, M.O., Pauz, V., Meinke, M., Schröder, W.: Computational analysis of nozzle geometry variations for subsonic turbulent jets. Comput. Fluids **136**, 467–484 (2016)
23. Ewert, R., Schröder, W.: Acoustic perturbation equations based on flow decomposition via source filtering. J. Comput. Phys. **188**(2), 365–398 (2003)
24. Koh, S.R., Geiser, G., Schröder, W.: Reformulation of acoustic entropy source terms. AIAA Paper, 2011–2927 (2011)
25. Markham, J.J.: Second-order acoustic fields: Streaming with viscosity and relaxation. Phys. Rev. **86**(4), 497 (1952)
26. Lintermann, A., Schlimpert, S., Grimmen, J.H., Günther, C., Meinke, M., Schröder, W.: Massively parallel grid generation on HPC systems. Comput. Methods Appl. Mech. Eng. **277**, 131–153 (2014)
27. Hartmann, D., Meinke, M., Schröder, W.: A strictly conservative cartesian cut-cell method for compressible viscous flows on adaptive grids. Comput. Methods Appl. Mech. Eng. **200**(9), 1038–1052 (2011)
28. Schneiders, L., Günther, C., Meinke, M., Schröder, W.: An efficient conservative cut-cell method for rigid bodies interacting with viscous compressible flows. J. Comput. Phys. **311**, 62–86 (2016)
29. Schneiders, L., Hartmann, D., Meinke, M., Schröder, W.: An accurate moving boundary formulation in cut-cell methods. J. Comput. Phys. **235**, 786–809 (2013)
30. Johansson, S.: High order finite difference operators with the summation by parts property based on DRP schemes. tech. Rep., 2004–036 (2004)
31. Hu, F.Q., Hussaini, M.Y., Manthey, J.L.: Low-dissipation and low-dispersion Runge-Kutta schemes for computational acoustics. J. Comput. Phys. **124**(1), 177–191 (1996)
32. Schröder, W., Ewert, R.: LES-CAA coupling. In: Large-eddy simulations for acoustics, Cambridge University Press (2005)
33. Ewert, R., Schröder, W.: On the simulation of trailing edge noise with a hybrid LES/APE method. J. Sound Vib. **270**(3), 509–524 (2004)

34. Pardowitz, B., Tapken, U., Knobloch, K., Bake, F., Bouty, E., Davis, I., Bennett, G.: Core noise–identification of broadband noise sources of a turbo-shaft engine. AIAA Paper, 2014–3321 (2014)
35. Siewert, C., Kunnen, R.P.J., Schröder, W.: Collision rates of small ellipsoids settling in turbulence. J. Fluid Mech. **758**, 686–701 (2014)
36. Kunnen, R.P.J., Siewert, C., Meinke, M., Schröder, W., Beheng, K.D.: Numerically determined geometric collision kernels in spatially evolving isotropic turbulence relevant for droplets in clouds. Atmos. Res. **127**, 8–21 (2013)
37. Bogey, C., Bailly, C.: Computation of a high Reynolds number jet and its radiated noise using large eddy simulation based on explicit filtering. Comput. Fluids **35**(10), 1344–1358 (2006)
38. Freund, J.B.: Proposed inflow/outflow boundary condition for direct computation of aerodynamic sound. AIAA J. **35**(4), 740–742 (1997)
39. Tam, C.K.W., Webb, J.C.: Dispersion-relation-preserving finite difference schemes for computational acoustics. J. Comput. Phys. **107**(2), 262–281 (1993)
40. Cetin, M.O., Koh, S.R., Meinke, M., Schröder, W.: Aeroacoustic analysis of a helicopter engine jet including a realistic nozzle geometry. AIAA Paper, 2015–2533 (2015)
41. Geiser, G., Koh, S., Schröder, W.: Analysis of acoustic source terms of a coaxial helium/air jet. AIAA Paper, 2011–2793 (2011)
42. Goldstein, M.E.: Aeroacoustics, vol. 1, p. 87. McGraw-Hill Inc., New York (1976)
43. Viswanathan, K.: Aeroacoustics of hot jets. J. Fluid Mech. **516**, 39–82 (2004)
44. Jülich Supercomputing Centre: JUQUEEN: IBM blue gene/Q supercomputer system at the jülich supercomputing centre. Journal of Large-Scale Research Facilities **1**(A1), A1 (2015). http://dx.doi.org/10.17815/jlsrf--1--18